Research on Chemical Intermediates (2020) 46:33–61
https://doi.org/10.1007/s11164-019-03934-w

Synthesis, characterization and investigation of photocatalytic activity of $ZnFe_2O_4$@MnO–GO and $ZnFe_2O_4$@MnO–rGO nanocomposites for degradation of dye Congo red from wastewater under visible light irradiation

Azam Zamani, et al. ***[full author details at the end of the article]***

Received: 22 May 2019 / Accepted: 16 July 2019 / Published online: 20 July 2019

Abstract

Magnetic $ZnFe_2O_4$@MnO–graphene oxide and $ZnFe_2O_4$@MnO–reduced graphene oxide nanocomposites were prepared via a facile co-precipitation and hydrothermal methods and characterized by X-ray powder diffraction, diffuse reflectance UV–Vis spectroscopy, photoluminescence (PL) spectra, Transmission electron microscopy, field emission scanning electron microscopy, Fourier transform infrared spectroscopy, vibrating sample magnetometry techniques and Bruner–Emmett–Teller (BET). The $ZnFe_2O_4$@MnO, $ZnFe_2O_4$@MnO–GO and $ZnFe_2O_4$@MnO–rGO nanoparticles were found to have a size of 20–40 nm and were spread out on the graphene oxide nanosheets and reduced graphene oxide nanosheets. Magnetic studies demonstrated that the $ZnFe_2O_4$@MnO–graphene oxide and $ZnFe_2O_4$@MnO–reduced graphene oxide nanocomposites can be easily separated from the solution by an external magnetic field. The photocatalytic degradation of Congo red dye (CR) was evaluated based on the removal of CR in aqueous solution in 35 min of visible light irradiation. The photocatalytic activity was affected by the structural and optical properties as well as the surface area of the samples. Compared with pure $ZnFe_2O_4$@MnO and $ZnFe_2O_4$@MnO–reduced graphene oxide nanocomposite, the $ZnFe_2O_4$@MnO–graphene oxide nanocomposite displayed a high photocatalytic activity on the photodegradation of Congo red. The prepared $ZnFe_2O_4$@MnO–graphene oxide nanocomposite can be potentially applied as a visible light responsive catalyst and magnetically separable photocatalyst and thus as a powerful separation tool for solving water pollution problems.

Keywords $ZnFe_2O_4$@MnO–graphene oxide nanocomposite · $ZnFe_2O_4$@MnO–reduced graphene oxide nanocomposite · Co-precipitation and hydrothermal methods · Photocatalytic activity · Degradation · Congo red

Introduction

Recent developments in the field of science and technology, particularly nanotechnology, have emerged the need for improvement in the synthesizing of nanosized particles of desired size and shape [1]. Synthetic dyes have been extensively employed in many manufactures such as paper, cloths, cosmetics, pharmaceuticals and printing as a colorant owing to their easy availability [2]. Dyes pollutants are transferred by adsorption onto the absorbent, and activated carbon is highly efficient in the removal of dyes [3]. This is significant because the acid functional group presence in azo and diazo dyes prevents them from being adsorbed by low-cost absorbent. However, activated carbon is not encouraging due to its heavy cost [4]. The conventional treatment is not a proper remedy for these environmental subjects; therefore, attention has been transferred to photocatalysis as a promising option to mineralized organic pollutants into CO_2, H_2O and mineral acid [5–7]. Various semiconductor photocatalysts have been reported for the degradation of organic pollutants. Among them, manganese oxide (MnO) is a semiconductor with a wide band gap width ($3.9 \pm 0/4$ eV) at room temperature [8]. Manganese oxides, including MnO, MnO_2, and Mn_3O_4, are intriguing composites and have been employed in wastewater treatment, catalysis, sensors, supercapacitors and alkaline and rechargeable batteries. Particularly, MnO and MnO_2 nanomaterials have attracted great interest as anode materials in Li-ion batteries (LIBs) for their high theoretical capacity, low cost, environmental benignity and special properties [9]. Zinc Ferrite ($ZnFe_2O_4$) exhibits superparamagnetic behavior, and it has potential application in many areas, such as photocatalysis, magnetic resonance imagery (MRI), Li-ion batteries and gas sensors [10]. Iron oxides are very common compounds and they are widespread in nature and readily synthesized in the lab. Almost everywhere of the global system atmosphere, biosphere, hydrosphere, and lithosphere, iron oxides present [11]. Graphene, an atomic sheet of sp^2 bonded carbon atoms, with remarkable electrical conductivity, high chemical and thermal stability, excellent adsorptivity, high transparency and large specific surface area, constitutes an excellent cloth for the adsorption of many pollutants [12]. Graphene oxide can be used as an ideal high-performance candidate for the charge migration during the photocatalysis process. Layers of graphene oxide consist of various oxidizing groups like hydroxyl, epoxides, carbonyl and carboxyl at the basal planes as good as at the edges. These groups can be reduced with the help of proper reducing agents to generate highly reduced graphene oxide sheets. In this study, we made an attempt to synthesize reduced graphene oxide films by oxidation of graphite to form graphene oxide followed by exfoliation and reduction in GO. The main difficulty of pure semiconductor photocatalysts is that the photogenerated electron–hole pairs have faster recombination rates, which will reduce the photocatalytic efficiency of the semiconductor photocatalysts [13, 14]. One of the effective ways to solve this problem is to prepare semiconductor nanocomposites, which will make simple the charge migration [15]. In recent years, metal oxide nanocomposites and nanocomposites based on graphene and graphene derivatives have been widely investigated, and

their photocatalytic properties have been reported such as GO–ZrO_2 nanocomposite (degrades rhodamine B 30 ppm in 105 min) [16], composite of $CoFe_2O_4$@TiO_2/rGO (decomposes chlorpyrifos 5 ppm in 60 min) [17], doping of Gd, C, N, S-ZrO_2 (decomposes indigo carmine 20 ppm in 210 min) [18], composite of Nd-ZrO_2–GO (degrades Eosin-Y 20 ppm in 180 min) [19], composite of $Ni_{0.4}Co_{0.6}Fe_2O_4$ (decomposes Congo red 10 ppm in 120 min) [20], MgO–ZrO2 nanocomposite (degrades basic blue 9 dye 5 ppm in 60 min) [21]. Despite a large number of articles published on nanocomposites photocatalytic activity, photocatalytic degradation of $ZnFe_2O_4$@MnO–graphene oxide and $ZnFe_2O_4$@MnO-reduced graphene oxide nanocomposites for degradation of Congo red dye under the visible light irradiation has not yet been reported. In this research, synthesis of the $ZnFe_2O_4$@MnO nanoparticles decorated on the surface reduced graphene oxide (RGO) and graphene oxide (GO). Therefore, nanocomposites ($ZnFe_2O_4$@MnO/RGO) and ($ZnFe_2O_4$@MnO/GO) were performed. Magnetic nanocomposites ($ZnFe_2O_4$@MnO/RGO) and ($ZnFe_2O_4$@MnO/GO) were synthesized by the hydrothermal and co-precipitation methods. The microstructure, optical properties and magnetic properties of the synthesized samples were investigated. Furthermore, percent degradation and degradation kinetics have been evaluated in detail.

Materials and methods

Materials

In the present experiment, all of the used chemicals were reagent grade such as graphite powder (99.99% purity), sulfuric acid (H_2SO_4, 98%), potassium permanganate ($KMnO_4$), hydrogen peroxide (H_2O_2, 30%), hydrochloric acid (HCl) and sodium hydroxide (NaOH, 20%) that chemical materials were purchased from Sigma-Aldrich Corporation (USA). Mn $(NO_3)_2$, Zn $(NO_3)_2$ and Fe $(NO_3)_3$ were purchased from the Merck corporation (Germany).

Instrumentation

The crystalline structure of $ZnFe_2O_4$@MnO/GO and $ZnFe_2O_4$@MnO/RGO was characterized by XRD (Philips PW 1730 Japan model) with CuK_α radiation (1.5406) Å in 2θ scan range of 10–80°. In order to examine the morphologies of $ZnFe_2O_4$@MnO/GO and $ZnFe_2O_4$@MnO/RGO nanoparticles, TEM measurements were performed on a Zeiss-EM10C-100 kV TEM instrument (Germany), and FESEM measurements were done with a ZEISS DSM-960A analytic microscope (Germany). PL emission spectra of the samples were analyzed at room temperature using a JASCO Spectrofluorometer (FP-8200). The specific surface area, pore distribution and pore parameters were studied by Brunauer–Emmet–Teller nitrogen adsorption–desorption isotherm at 77 k using Belsorp mini II instrument. Then, a diffuse reflectance spectrum (DRS) of the $ZnFe_2O_4$@MnO/GO and $ZnFe_2O_4$@

MnO/RGO nanocomposites was recorded on a UV-2550 Shimadzu UV–Vis spectrophotometer equipped with ISR-2200 DRS accessory (UV-2550 Shimadzu, Japan). Finally, IR spectra were recorded on a Bruker FT-IR instrument using KBr plates.

Synthesis of the $ZnFe_2O_4$@MnO nanoparticles

$ZnFe_2O_4$@MnO nanoparticles are synthesized by a co-precipitation method [17]. In this consideration, 3.75 g Zn $(NO_3)_2$ and 4.87 g Fe $(NO_3)_3$ dissolved in 40 ml of distilled water were mixed under magnetic stirring for 10 min. Then, 20% NaOH was added dropwise into solution, and the pH level was maintained above 10 under stirring for 15 min. Then, a dark brown suspension was obtained. In addition, 1 g of MnO was calcined at 400 °C for 5 h. Then, the calcined MnO was added to 20% NaOH solution and magnetically stirred for 10 min. After the Zn–Fe precursor solution was added to the suspension, the new mixture was stirred for 30 min in the dark at 90 °C for 1 h. In the next stage, the obtained residue was filtered and washed with ultrapure water for several times and dried at 70 °C overnight. Finally, the residue was calcined at 500 °C for 3 h to form $ZnFe_2O_4$@MnO nanoparticles.

Synthesis of graphene oxide

Graphene oxide (GO) was synthesized from natural graphite flake via modified Hummer's method [22]. In a typical synthesis, 9 g of graphite flake was added in 25 ml of sulfuric acid (98%), and the mixture was sonicated to produce a fine dispersion. Then, this suspension was heated for 6 h at 80 °C under magnetic stirring. 30 g of potassium permanganate was added slowly to the mixture during the stirring process. The mixture was cooled to below 10 °C. Further, the mixture was stirred under ice water bath for two hours. This solution was diluted with distilled water and treated with 20 ml of hydrogen peroxide (30%) and was kept undisturbed for 24 h for precipitation. The resulting GO solution was washed several times with hydrochloric acid and distilled water using a centrifuge.

Synthesis of reduced graphene oxide

To obtain reduced graphene oxide, hydrazine hydrate was used as the reducing agent. The as-prepared GO was dispersed into 200 ml water under mild ultrasound yielding a yellow–brown suspension. Then, 4 ml of hydrazine hydrate (80 wt.%) was added dropwise, and the solution was heated in a water bath for 24 h at 80 °C. After the reaction, the prepared rGO product was washed with distilled water and collected by vacuum filtration.

Synthesis of the $ZnFe_2O_4$@MnO/GO nanoparticles

The hydrothermal method was employed to synthesize the $ZnFe_2O_4$@MnO–graphene oxide nanocomposites [23]. 1000 mg of GO was dispersed in 50 ml of distilled water with sonication for 1 h, and then 200 mg $ZnFe_2O_4$@MnO suspension

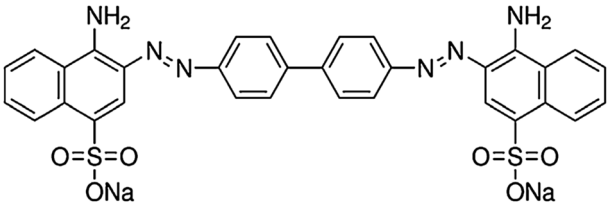

Fig. 1 Chemical formula of CR

was added and the mixture stirred for 30 min at room temperature to produce a $ZnFe_2O_4$@MnO–GO dispersion. The mixture was transferred to a 100 ml Teflon-lined stainless steel autoclave and heated to 200 °C for 5 h under autogenous pressure. The reaction mixture was allowed to cool to room temperature and the residue was filtered, washed with distilled water and dried in a vacuum oven at 60 °C for 12 h.

Synthesis of the $ZnFe_2O_4$@MnO/rGO nanoparticles

The hydrothermal method was used to synthesize the ZnFe2O4@MnO-reduced graphene oxide nanocomposites [23]. 1000 mg of rGO was dispersed in 50 ml of ultrapure water with ultrasonication for 1 h to form a stable rGO suspension, and then 200 mg $ZnFe_2O_4$@MnO suspension was added and the mixture stirred for 30 min at room temperature to produce a $ZnFe_2O_4$@MnO–rGO dispersion. The mixture was transferred to a 100 ml Teflon-lined stainless steel autoclave and heated to 200 °C for 5 h under autogenous pressure. The reaction mixture was allowed to cool to room temperature and the residue was filtered, washed with ultrapure water and ethanol. Then, residues were dried in a vacuum oven at 60 °C for 12 h.

Photocatalytic degradation experiments

Photocatalytic activities of $ZnFe_2O_4$@MnO–graphene oxide and $ZnFe_2O_4$@MnO-reduced graphene oxide nanocomposites were measured by monitoring the degradation rate of CR solution. In order to provide desired visible light, a batch system was employed to carry out the photocatalytic degradation of CR. (Figure 1 shows the chemical formula of CR.) 0. 10 g l^{-1} of $ZnFe_2O_4$@MnO–graphene oxide and $ZnFe_2O_4$@MnO- reduced graphene oxide was investigated under irradiation of 5 W white LED lamp. The photocatalytic experiments were performed at 25 °C with a concentration of 0. 10 g l^{-1} catalysts and 10 mg l^{-1} of CR solution with time intervals of (5–35 min) at pH = 4. In this experiment, 0.10 g l^{-1} of $ZnFe_2O_4$@MnO, $ZnFe_2O_4$@MnO–rGO and $ZnFe_2O_4$@MZnO-GO nanocomposites was added to 100 ml of (10 mg l^{-1}) CR solution. Before the photocatalytic reaction, the suspension was stirred in the dark for 30 min for adsorption–desorption equilibrium between the photocatalyst and dye solution. Finally, it was irradiated. During irradiation, 5 ml of the suspension was sampled at an interval of 5 min and centrifuged to eliminate the catalyst particles and it was measured by Shimadzu UV-1650PC

Model UV–Vis spectrophotometer at $\lambda_{max} = 500$ nm. The dye degradation percentage was obtained from the following equation:

$$R = (C_0 - C)/C_0 * 100 \quad (1)$$

where C_0 represents the initial CR concentration (mg/l) and C indicates the CR concentration at a certain reaction time (min). The kinetic studies were performed at 25 °C with a concentration range of 0. 10 g l^{-1}, 0.05 g l^{-1} and 0.020 g l^{-1} $ZnFe_2O_4$@MnO–rGO and $ZnFe_2O_4$@MZnO-GO nanocomposites and 10 mg l^{-1} of CR solution with times intervals of (5–35 min) at pH = 4.

Results and discussion

Structural study

XRD patterns of the samples were recorded in ambient air by using a Philips Xpert XRD. Figures 2 and 3 illustrate the X-ray diffraction patterns of the as-prepared $ZnFe_2O_4$@MnO–GO, $ZnFe_2O_4$@MnO–rGO, GO, rGO and pure $ZnFe_2O_4$@MnO in the 2θ ranges from 5° to 80°. The average crystallite size for $ZnFe_2O_4$@MnO–GO, $ZnFe_2O_4$@MnO–rGO and pure $ZnFe_2O_4$@MnO from the range of 20–40 nm was calculated by using standard Debye–Scherrer equation $D = 0.9\ \lambda/(\beta\cos\theta)$ [24], where D indicates the diameter of the nanoparticles, λ (Cu Kα) = 1.5406 Å and β represents the full-width at half maximum of the diffraction lines. Figure 2 displays the X-ray diffraction pattern of the GO, pure $ZnFe_2O_4$@MnO and $ZnFe_2O_4$@MnO–GO, respectively. As shown in Fig. 2a, GO diffraction peaks at the angles of 11.89°, 26.61°, 44.39° and 77.24° indicated (001), (002), (101) and (110), respectively, which confirmed the hexagonal phase and were directly matched with standard (JCPDS No.00 -041-1487). The

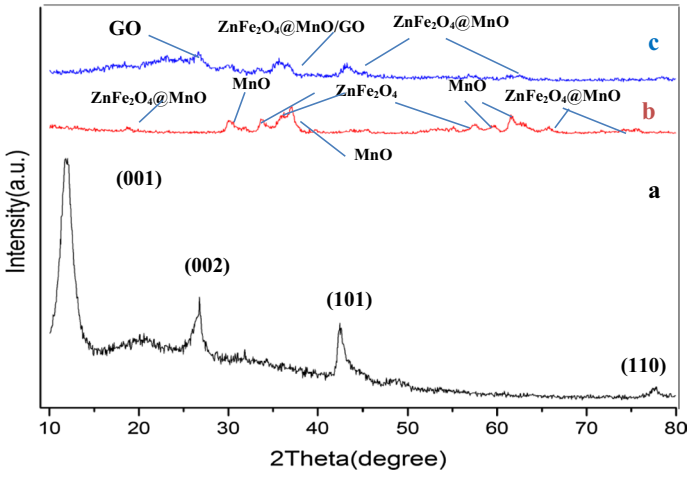

Fig. 2 XRD patterns for (a) GO, (b) $ZnFe_2O_4$@MnO and (c) $ZnFe_2O_4$@MnO/GO

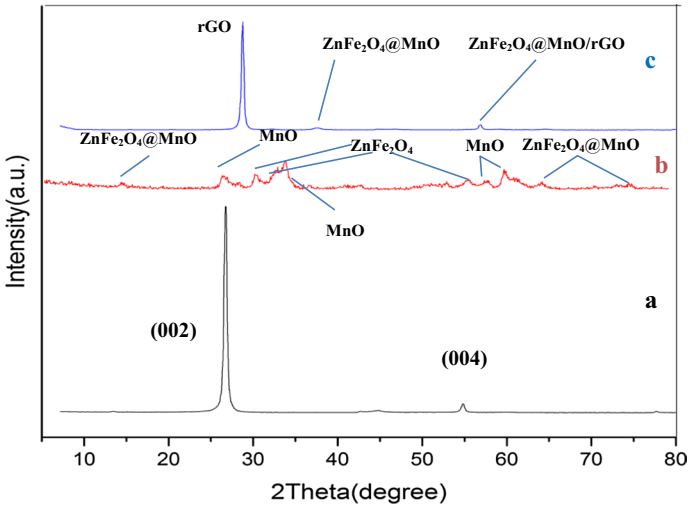

Fig. 3 XRD patterns for (a) rGO, (b) $ZnFe_2O_4$@MnO and (c) $ZnFe_2O_4$@MnO/rGO

X-ray diffraction pattern of GO displays an intense and sharp peak centered at 11.89° which corresponds to an interplanar distance of 0.82 nm. The increase in interplanar distance of GO is owing to the existence of oxygen functional groups and some other structural flaws. The detectable (002) peak of graphite at 26.61° has an interplanar distance of 0.334 nm. This indicates that graphite is a very oriented carbon material. Also, two other peaks at 44.39° and 77.24° imply the crystalline structure of graphite [25]. The X-ray diffraction pattern of $ZnFe_2O_4$@MnO is shown in Fig. 2b. The peaks centered at the angles of 18.24°, 57.42° and 75.50° indicated (111), (511) and (171), respectively, correspond to $ZnFe_2O_4$@MnO. Based on the results, the peaks centered at the angles of 35.34°, 56.79°, 62.36° and 73.76° indicated (311), (511), (400) and (533) concurred to the cubic phase of $ZnFe_2O_4$ which were directly indexed to JCPDS No. 98-003-0547. The peaks centered at the angles of 29.96°, 33.52°, 37.88°, 42.19°, 57.84°, 64.43° and 65.38° indicated (023), (113), (006), (220) and (212) agreed to the cubic phase of MnO which were directly indexed to JCPDS No. 01-075-0257. Figure 2c displays the X-ray diffraction pattern of the $ZnFe_2O_4$@MnO–GO. The peaks centered at the angles of 26.45°, 29.87° and 43.41° corresponded to GO, $ZnFe_2O_4$@MnO–GO and $ZnFe_2O_4$@MnO, respectively. On the other hand, during the hydrothermal reaction, crystal growth of ZnFe2O4@MnO between the interplay of GO damaged the regular layer stacking, making to the exfoliation of GO and the disappearance of the (001) diffraction peak [23]. Figure 3 displays the X-ray diffraction pattern of the rGO, pure $ZnFe_2O_4$@MnO and $ZnFe_2O_4$@MnO–rGO, respectively. As shown in Fig. 3a, rGO diffraction peaks at the angles of 26.60 and 54.79° attributed to (002) and (004), respectively, which confirmed the hexagonal phase and were directly matched with standard (JCPDS No.00 -025-0284). On the other hand, a broad peak shown at $2\theta = 26.60°$, which can be corresponded to an interplanar distance of 0.33 nm along the (002) orientation.

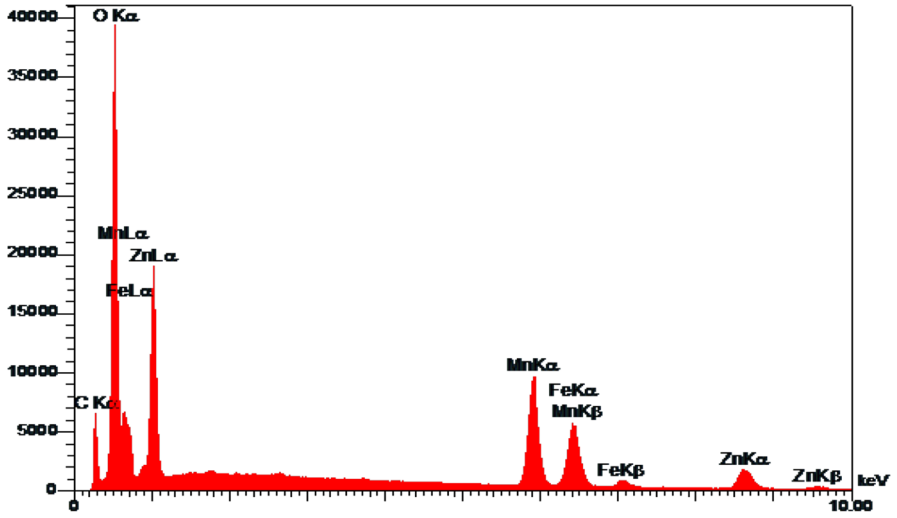

Fig. 4 EDAX analyses of $ZnFe_2O_4$@MnO–GO nanocomposite

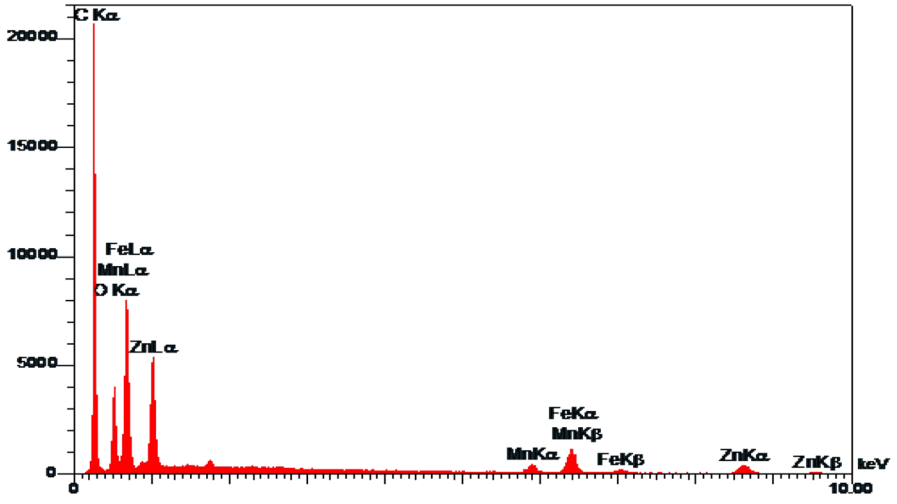

Fig. 5 EDAX analyses of $ZnFe_2O_4$@MnO–rGO nanocomposite

This can be described by the removal of oxygen functional groups, leading to a decrease in d-spacing [26]. The X-ray diffraction pattern of $ZnFe_2O_4$@MnO is shown in Fig. 3b. Figure 3c shows the X-ray diffraction pattern of the $ZnFe_2O_4$@MnO–rGO. The peaks centered at the angles of 26.63°, 35.64° and 56.91° attributed to rGO, $ZnFe_2O_4$@MnO and $ZnFe_2O_4$@MnO–rGO, respectively. As illustrated in Figs. 4 and 5, the EDAX data for the nanocatalyst $ZnFe_2O_4$@MnO–GO and $ZnFe_2O_4$@MnO–rGO could confirm the presence of C, Zn, Fe, Mn and O elements in synthesized photocatalysts, respectively. The amounts of elements

Table 1 EDX quantification elements of $ZnFe_2O_4$@MnO–GO nanocomposite

Element	C	O	Mn	Fe	Zn	Total
Wt%	12.54	33.94	25.60	13.28	14.65	100.00
Atom%	25.50	51.83	11.39	5.81	5.47	100.00

Table 2 EDX quantification elements of $ZnFe_2O_4$@MnO–rGO nanocomposite

Element	C	O	Mn	Fe	Zn	Total
Wt%	58.63	28.24	3.42	7.44	2. 27	100.00
Atom%	71.02	25.68	0.76	1.94	0.60	100.00

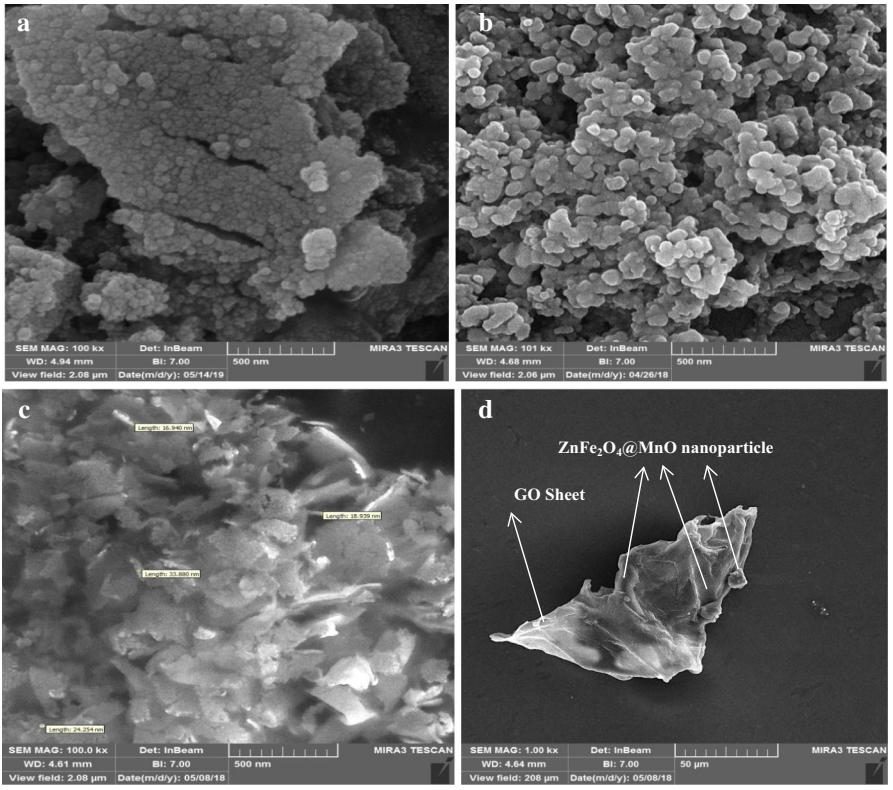

Fig. 6 **a** FESEM image of GO sheets, **b** $ZnFe_2O_4$@MnO nanoparticles, **c** and **d** $ZnFe_2O_4$@MnO–GO nanocomposites

are reported for the nanocatalyst $ZnFe_2O_4$@MnO–GO and $ZnFe_2O_4$@MnO–rGO in Tables 1 and 2, respectively. Further, as shown in Figs. 6 and 7, the surface morphology and its chemical composition of the synthesized photocatalysts were analyzed by FESEM image. Figure 6a confirms the formation of a multilayered of GO nanosheet, while Figs. 6b and 7b display the agglomerated

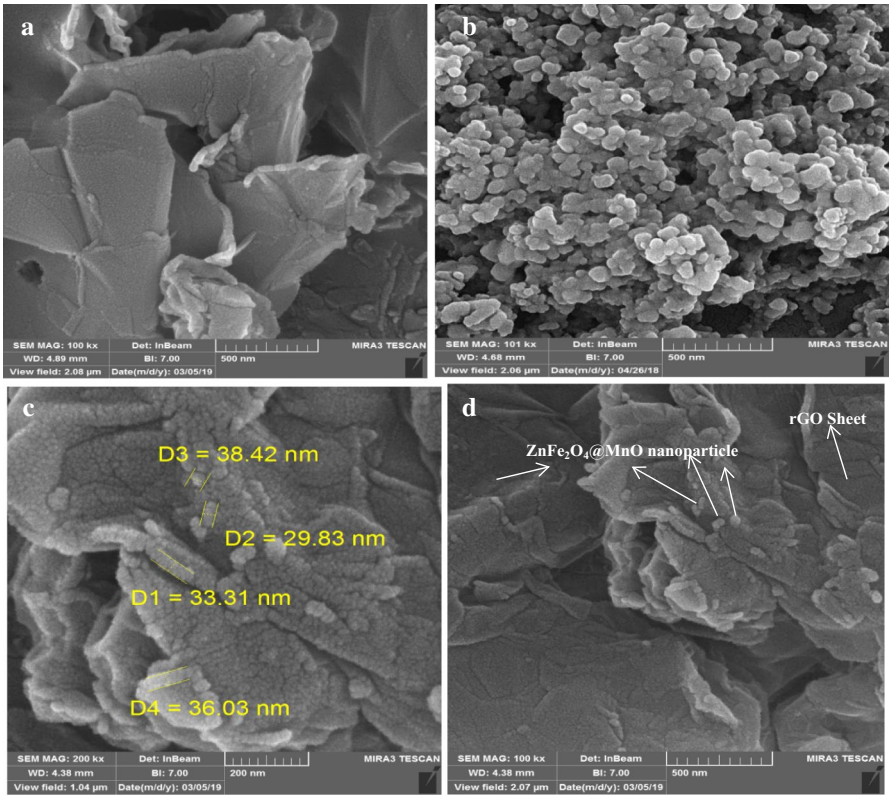

Fig. 7 **a** FESEM image of rGO sheets, **b** $ZnFe_2O_4$@MnO nanoparticles, **c** and **d** $ZnFe_2O_4$@MnO–rGO nanocomposites

spherical shape of $ZnFe_2O_4$@MnO nanoparticles with an average particle size of ˂100 nm. Furthermore, it can be shown that the spherical shape of $ZnFe_2O_4$@MnO nanoparticles was unequally decorated on the surface of the GO sheet with an average particle size of ˂100 nm in Fig. 6c, d. Figure 7a confirms reduced graphene oxide wrinkled structure that induced sheet folding [26]. Furthermore, Fig. 7c, d displays that the surface of the rGO sheet was well-decorated with $ZnFe_2O_4$@MnO nanoparticles with the formation of spherical shape and with an average particle size of ˂100 nm. The TEM images of the $ZnFe_2O_4$@MnO–GO and $ZnFe_2O_4$@MnO–rGO nanocomposites are shown in Figs. 8 and 9. It can be clearly shown that the microstructure of $ZnFe_2O_4$@MnO–GO samples display the agglomerated spherical $ZnFe_2O_4$@MnO nanoparticles, which are randomly dispersed over the surface of GO nanosheets as shown in Fig. 8. Also, Fig. 9 displays the spherical shape microstructure of $ZnFe_2O_4$@MnO–rGO nanomaterials, which are randomly dispersed over the surface of rGO sheets. Additionally, the dark gray nanoparticles ($ZnFe_2O_4$) were dispersed on the surface of light gray nanoparticles (MnO) as shown in Figs. 8 and 9.

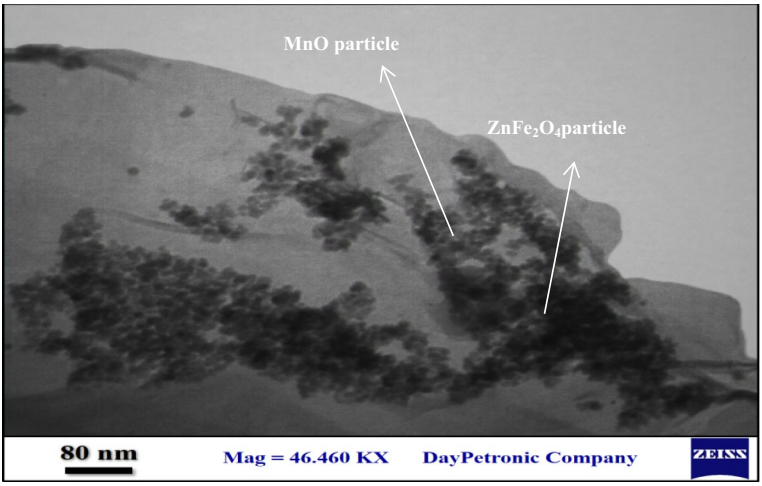

Fig. 8 TEM images of the $ZnFe_2O_4$@MnO–GO nanocomposites

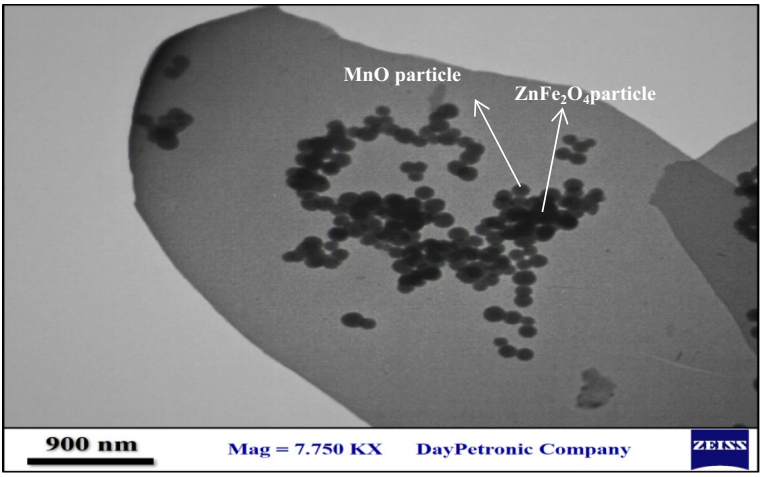

Fig. 9 TEM images of the $ZnFe_2O_4$@MnO–rGO nanocomposites

Infrared spectral study

FT-IR analysis was applied to investigate the surface chemical compositions of the obtained samples in the synthesized GO, $ZnFe_2O_4$@MnO–GO and ZnFe2O4@MnO as shown in Fig. 10. As shown, the solid-state FT-IR spectra of the nanocomposites indicating a low intensity bands in the range of 480 and 507 cm^{-1} were assigned to Zn–O and Mn–O stretching vibrations, respectively. In addition, another peak appeared at the 650–540 cm^{-1}, which could be attributed to the Fe–O stretching. The absorption band around 1707 cm^{-1} assigned to

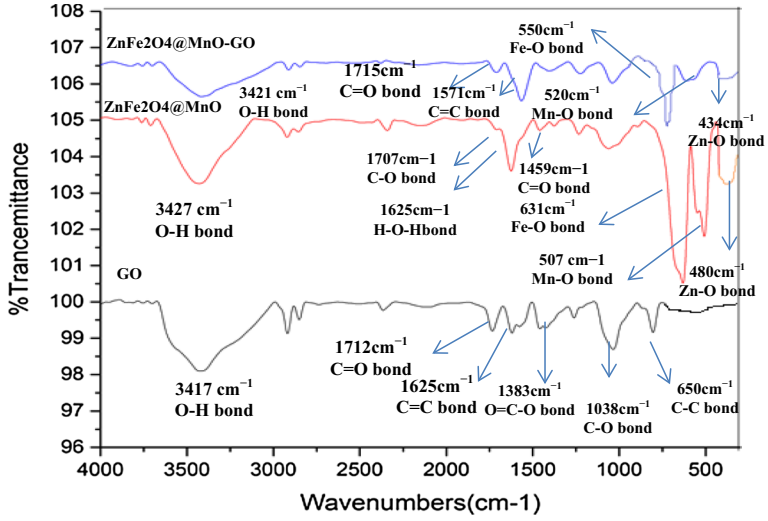

Fig. 10 FT-IR spectra of prepared GO, $ZnFe_2O_4$@MnO and $ZnFe_2O_4$@MnO–GO nanocomposites

stretching vibration of carbonyl group C–O. The stretching vibration of the carboxylate group C=O is shown around 1459 cm^{-1}. Also, the bending vibration of H–O–H group appeared at 1625 cm^{-1}. The band at 3500–3200 cm^{-1} is attributed to the stretching and bending modes of free and absorbed water on the surface of the synthesized $ZnFe_2O_4$@MnO nanocomposites [23]. The FT-IR spectra confirm the presence of organic impurities in sample owing to the preparation conditions. For the graphene oxide spectrum, the peak at 1038 cm^{-1} which is assigned to the C–O bond, confirming the presence of oxide functional groups after the oxidation process. The peaks in the range of 1625–1650 cm^{-1} display that the C=C bond yet stayed before and after the oxidation process. The peaks around 1200–1380 cm^{-1} were related to various C–H stretching vibrations. Another peak around 650–850 cm^{-1} is related to C–C out of plane bending. The broad peak at 3417–3715 cm^{-1} is assigned to the O–H stretch of H_2O molecules. This supports the principle that GO is a highly absorptive material, as confirmed by its ability to become a solution similar to gel. The spectrum of $ZnFe_2O4$@MnO–GO nanocomposites shows the distinctive peaks owing to $ZnFe_2O_4$@MnO and graphene oxide at 430–600 cm^{-1} and 3400 cm^{-1}, respectively, and also, the bands around 1380 cm^{-1} and 1038 cm^{-1}, which could be attributed to the oxygen functional groups on the graphene oxide sheet [25]. Figure 11 shows the FT-IR spectra of rGO, $ZnFe_2O_4$@MnO–rGO and $ZnFe_2O_4$@MnO nanocomposites. The FT-IR spectrum of rGO displayed no sharp peaks attributing to the oxygen functionalities which confirm the efficient reduction in GO into rGO. Stretching vibrations of O–H groups at 3400 cm^{-1} were missing due to deoxygenation, though stretching vibration around 2600–2800 cm^{-1} was assigned to the presence of C–H groups, even after the reduction process and stretching vibrations around 1600 cm^{-1}, which can be related to the graphitic domains certifying the formation

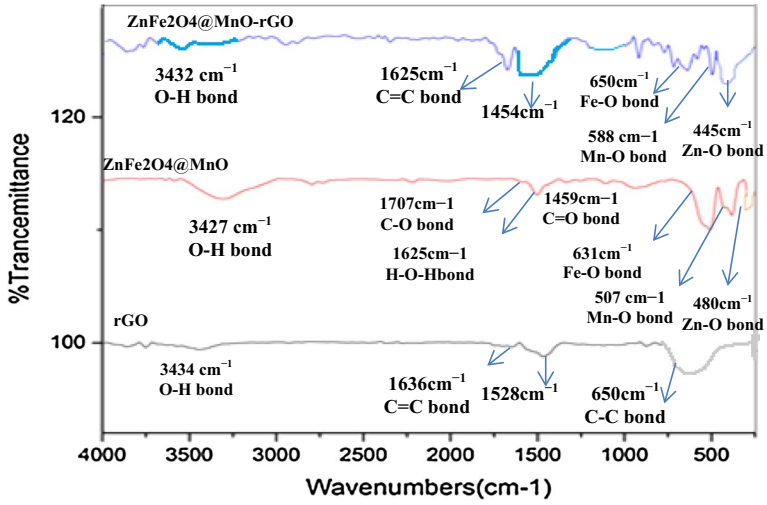

Fig. 11 FT-IR spectra of prepared rGO, $ZnFe_2O_4$@MnO and $ZnFe_2O_4$@MnO–rGO nanocomposites

of sp^2 carbon structure of rGO. The peak in the range of 1450–1583 cm^{-1} appears that may be attributed to the skeletal vibration of the reduced graphite oxide [27]. The FT-IR bands of ZnFe2O4@MnO–rGO are observed in the ranges 1200–1380 cm^{-1} and 1625 cm^{-1}, which can be corresponded to C–H groups and C=C bond stretching vibrations, respectively. In addition, another peak appeared at the 445 $cm^{-1,}$ 588 cm^{-1} and 650 cm^{-1} which could be attributed to Zn–O, Mn–O and Fe–O stretching vibrations, respectively.

Magnetic properties of $ZnFe_2O_4$@MnO–GO and $ZnFe_2O_4$@MnO–rGO

The magnetization measurement for the prepared $ZnFe_2O_4$@MnO, $ZnFe_2O_4$@MnO–GO and $ZnFe_2O_4$@MnO–rGO nanocomposites was recorded by employing the vibrating sample magnetometer (VSM) at room temperature. The magnetic hysteresis loops of the synthesized $ZnFe_2O_4$@MnO and $ZnFe_2O_4$@MnO–GO nanocomposites are shown in Fig. 12, which demonstrates that the resulting samples revealed a characteristic of the superparamagnetic behavior with the saturation magnetization of 1.26 and 0.91 emu g^{-1} of $ZnFe_2O_4$@MnO and $ZnFe_2O_4$@MnO–GO nanocomposites, respectively. Figure 13 illustrates the hysteresis loops of the $ZnFe_2O_4$@MnO and $ZnFe_2O_4$@MnO–rGO nanocomposites. The results demonstrated the superparamagnetic behavior of the prepared samples with the saturation magnetization of 1.26 and 1.43 emu g^{-1} of $ZnFe_2O_4$@MnO and $ZnFe_2O_4$@MnO–rGO nanocomposites, respectively. Finally, the results confirmed the superparamagnetic behavior of the prepared samples because of a decrease in the crystallite size below a critical value (lower than 100 nm). Therefore, the size of the crystalline nature influences the magnetic properties of the nanoparticles [28].

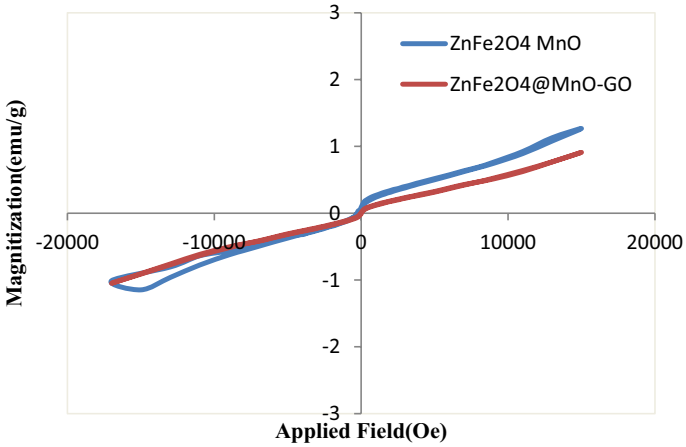

Fig. 12 Hysteresis curves of $ZnFe_2O_4$@MnO and $ZnFe_2O_4$@MnO–GO nanocomposites

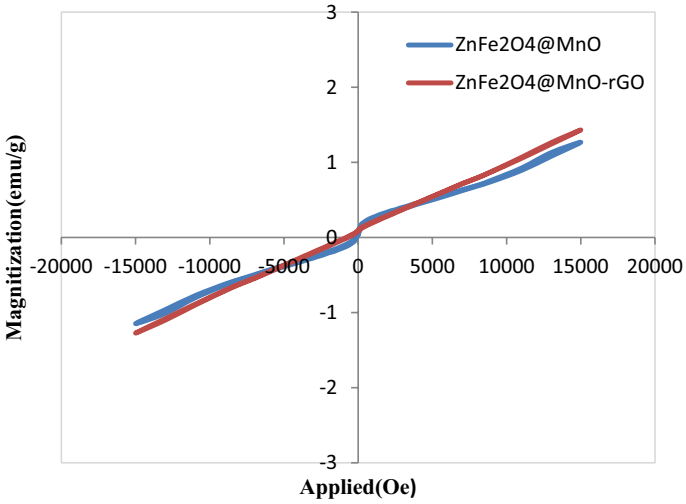

Fig. 13 Hysteresis curves of $ZnFe_2O_4$@MnO and $ZnFe_2O_4$@MnO–rGO nanocomposites

Optical analysis of $ZnFe_2O_4$@MnO–GO and $ZnFe_2O_4$@MnO–rGO

The optical absorption property related to the electronic structure formation is identified as a key factor in demonstrating the photocatalytic activity [29]. The optical properties of the synthesized $ZnFe_2O_4$@MnO, $ZnFe_2O_4$@MnO–GO and $ZnFe_2O_4$@MnO–rGO samples were studied by the diffused reflectance UV–Vis spectra (DRS) of the prepared samples, as shown in Figs. 14 and 15. According to the spectra, all synthesized samples displayed photoabsorption from UV light to visible light region, which shows the possibility of high photocatalytic activity of these nanocomposites

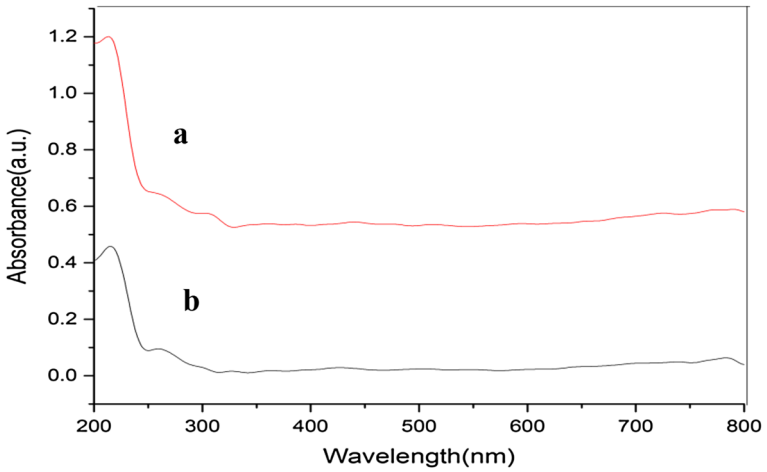

Fig. 14 Optical Absorption Spectrum of **a** $ZnFe_2O_4$@MnO and **b** $ZnFe_2O_4$@MnO–GO

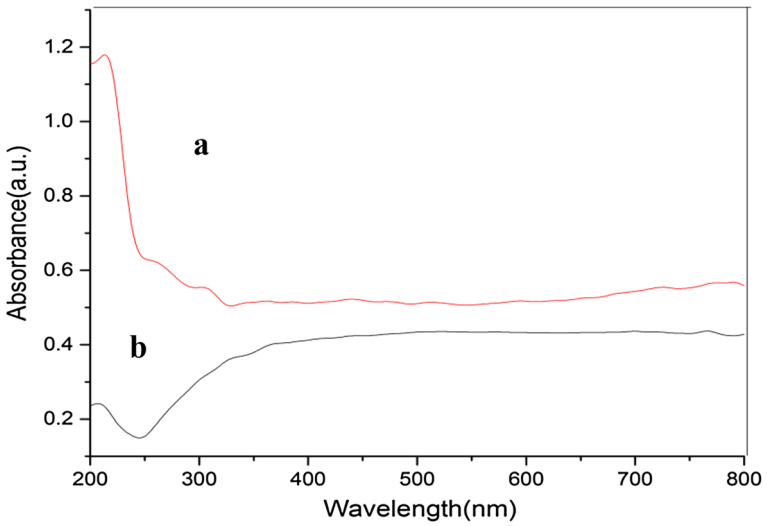

Fig. 15 Optical Absorption Spectrum of **a** $ZnFe_2O_4$@MnO and **b** $ZnFe_2O_4$@MnO–rGO

under visible light. The band gap of the synthesized materials calculated from the plot of the transformed Kubelka-Munck function versus the energy of light [30] is shown in Figs. 16 and 17. The band gap energies of the synthesized $ZnFe_2O_4$@MnO, $ZnFe_2O_4$@MnO–GO and $ZnFe_2O_4$@MnO–rGO nanocomposites are 3.78, 3.29 eV and 5 eV, respectively. As mentioned above, the addition of GO causes the band gap narrowing of $ZnFe_2O_4$@MnO to 3.29 eV for $ZnFe_2O_4$@MnO–GO. However, this band gap is yet so large that visible light irradiation ($\lambda > 420$ nm) cannot photoexcite electrons in the valence band (VB) to the conduction band (CB) of $ZnFe_2O_4$@MnO.

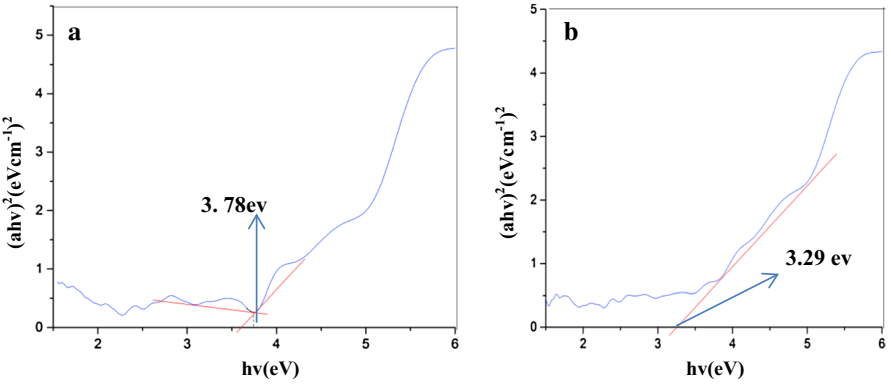

Fig. 16 DRS plots of $(ahv)^2$ versus photon energy hv (eV) for **a** $ZnFe_2O_4$@MnO and **b** $ZnFe_2O_4$@MnO–GO

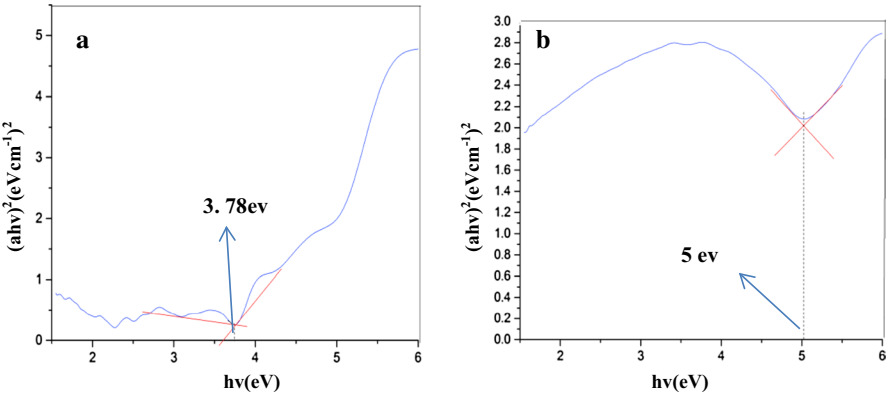

Fig. 17 DRS plots of $(ahv)^2$ versus photon energy hv (eV) for **a** $ZnFe_2O_4$@MnO and **b** $ZnFe_2O_4$@MnO–rGO

From the old photocatalysts of semiconductor_C_{60} and semiconductor_carbon nanotube (CNT) [31, 32], we could conclude the feasible indications to infer that GO acts as a visible light photosensitizer to $ZnFe_2O_4$@MnO in the nanocomposite of $ZnFe_2O_4$@MnO–GO. In other words, under visible light irradiation, photoexcited electrons are generated from GO and then transferred to the CB of $ZnFe_2O_4$@MnO, which hence transforms wide band gap $ZnFe_2O_4$@MnO to a visible light photocatalyst. Such a similar photocatalytic reaction mechanism has been proposed in previous semiconductor_ C_{60} or _CNT visible light photocatalysts [31–34]. For example, Kamat et al. have found that for the C_{60}_TiO_2 photocatalyst, C_{60} can be photoexcited under visible light laser beam irradiation, and the photoinduced electrons can be transferred to the CB of TiO_2 [33]. However, these chemical models promote us to imagine that for $ZnFe_2O_4$@MnO/GO photocatalyst, the role of GO could act as a macromolecular "photosensitizer" for $ZnFe_2O_4$@MnO, hence making it display

visible light photoactivity [35]. Additionally, the addition of rGO causes increase in the band gap width of $ZnFe_2O_4$@MnO to 5 eV for $ZnFe_2O_4$@MnO–rGO. Thus, this band gap is so large that visible light irradiation ($\lambda > 420$ nm) cannot photoexcite electrons in the valence band (VB) to the conduction band (CB) of $ZnFe_2O_4$@MnO. On the other hand, $ZnFe_2O_4$@MnO shows strong bonding interaction with GO moiety rather than rGO due to the presence of a large number of oxygen containing the functional group. This is supported by the improved photocatalytic properties of the synthesized $ZnFe_2O_4$@MnO/GO nanocomposite compared to the $ZnFe_2O_4$@MnO/rGO nanocomposite under the under the visible light [36].

Porosity and Surface Chemistry of $ZnFe_2O_4$@MnO–GO and $ZnFe_2O_4$@MnO–rGO

The nitrogen adsorption–desorption isotherms were performed in order to carry out an analysis relevant to the porosity properties of $ZnFe_2O_4$@MnO–GO and $ZnFe_2O_4$@MnO–rGO, and the further interpretation was performed by using Brunauer–Emmett–Teller (BET) method. Total pore volume, average pore diameters and surface area of synthesized samples, for evaluation of porosity and surface chemistry are listed in Table 2. Figures 18 and 19 display the N_2 adsorption isotherm and pore size distribution curve of synthesized $ZnFe_2O_4$@MnO–GO and $ZnFe_2O_4$@MnO–rGO nanocomposites. The isotherms show the features of type IV isotherms according to IUPAC classification, indicating the presence of mesopores structures in the samples. The specific surface area of $ZnFe_2O_4$@MnO–GO and $ZnFe_2O_4$@MnO–rGO nanocomposites are 26.77 m^2/g and 14.08 m^2/g with an average pore size diameter of 18.03 nm and 18.83 nm, respectively, which significantly determines the mesoporous nature, while the surface area of $ZnFe_2O_4$@MnO nanoparticles, GO and rGO are found to be 75.54 m^2/g, 5.86 m^2/g and 11.01 m^2/g with an average pore size of 10.74 nm, 25.37 nm and 19.24 nm, respectively, as given in Table 3. The lower surface area of $ZnFe_2O_4$@MnO–GO and $ZnFe_2O_4$@MnO–rGO nanocomposites compared to the $ZnFe_2O_4$@MnO may be owing to blocking of a few sites by GO and rGO in the $ZnFe_2O_4$@MnO structure [16]. On the other hand, the surface area of the catalyst is one of the most important factors in photodegradation processes; higher surface area of the catalyst causes the generation of more active species and improvement of the photocatalytic performance [37]. The higher surface area of synthesized $ZnFe_2O_4$@MnO–GO compared to the $ZnFe_2O_4$@MnO–rGO causes the generation improvement of the photocatalytic activity of the synthesized $ZnFe_2O_4$@MnO–GO nanocomposite compared to the $ZnFe_2O_4$@MnO–rGO nanocomposite under the visible light.

Photoluminescence

The recombination rate of the photogenerated electron–hole pair in the semiconductor materials was studied through photoluminescence (PL) spectroscopic analysis as shown in Figs. 20 and 21. The PL emission spectra of $ZnFe_2O_4$@MnO–GO and $ZnFe_2O_4$@MnO–rGO nanocomposites and $ZnFe_2O_4$@MnO were recorded in excitation wavelength of 358 nm at room temperature and the

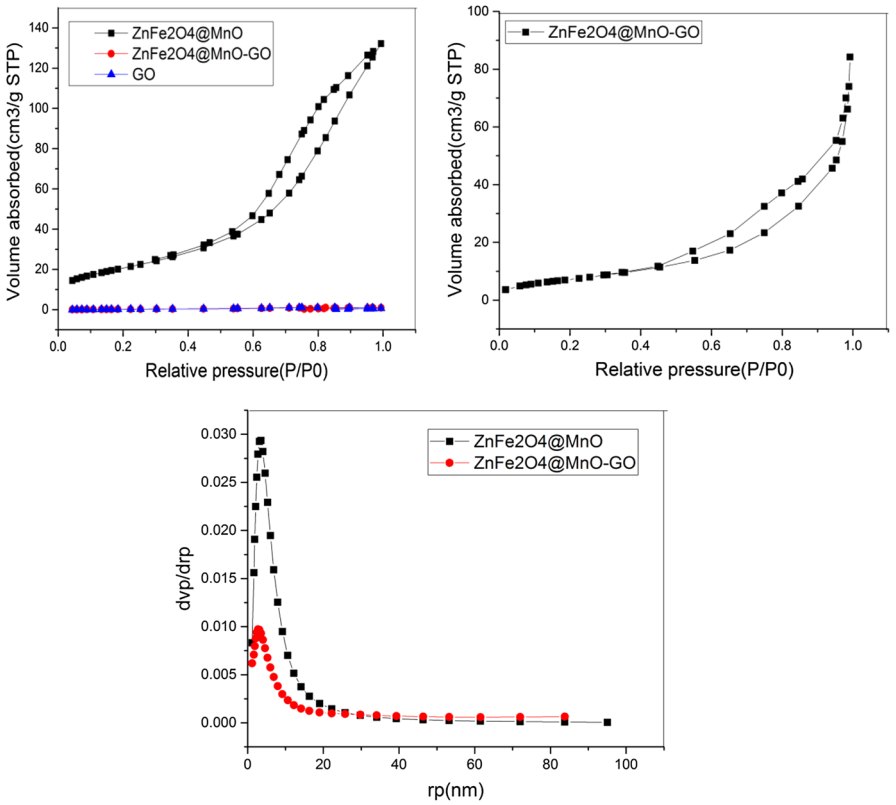

Fig. 18 N_2 adsorption isotherms of GO, $ZnFe_2O_4$@MnO and $ZnFe_2O_4$@MnO–GO nanocomposites along with pore size distribution curve

emission spectra emerged at 558 nm, 554 nm and 560 nm, showing a small blue shift, which reveals a good interaction between the metal oxide and GO. These findings explained the existence of efficient separation of photogenerated charge carrier owing to the decreasing intensity of synthesized $ZnFe_2O_4$@MnO–GO nanocomposite in PL spectra, which repressed the recombination rate of e^-/h^+ pairs and increase the photocatalytic degradation rate of organic pollutants. The mechanism involved is when $ZnFe_2O_4$@MnO nanomaterials are decorated on the surface of GO; the photogenerated electrons on the conduction band (CB) of $ZnFe_2O_4$@MnO transfer to the GO sheet. The presence of a conjugated π-system in GO delocalized the electrons on the surface of the GO sheet. This findings in enhanced separation of e^-/h^+ pairs lead to enhance the photocatalytic performance in the case of synthesized $ZnFe_2O_4$@MnO–GO nanocomposite as compared to their naked counterparts ($ZnFe_2O_4$@MnO and GO). Additionally, $ZnFe_2O_4$@MnO also shows strong bonding interaction with GO moiety rather than rGO owing to the presence of a large number of oxygen containing the

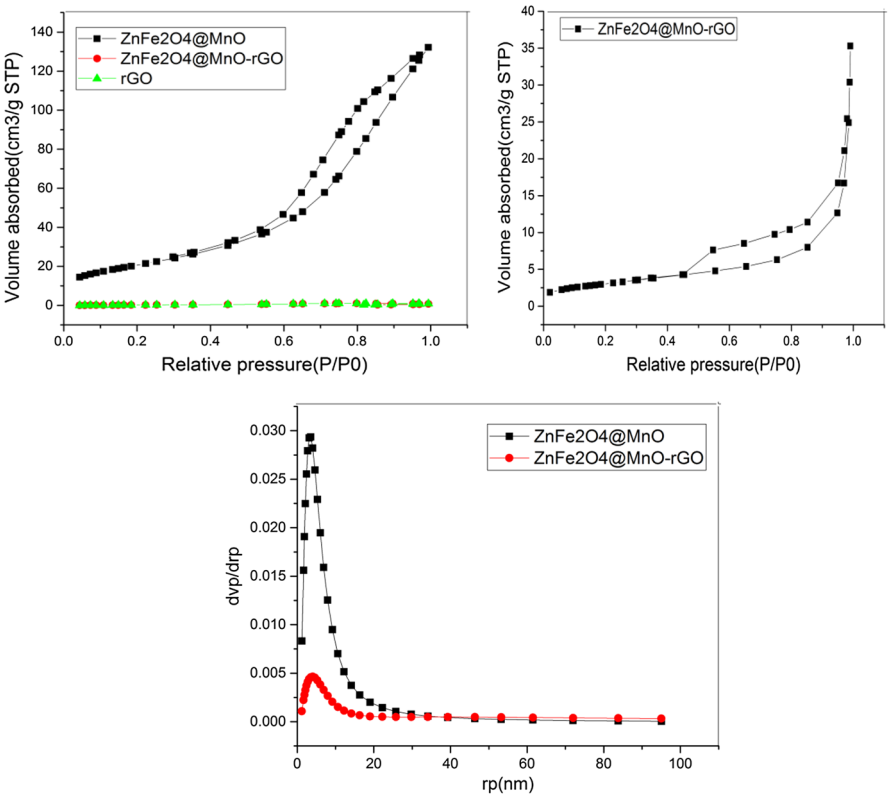

Fig. 19 N_2 adsorption isotherms of rGO, $ZnFe_2O_4$@MnO and $ZnFe_2O_4$@MnO–rGO nanocomposites along with pore size distribution curve

Table 3 BET analysis of GO, rGO, $ZnFe_2O_4$@MnO, $ZnFe_2O_4$@MnO–GO and $ZnFe_2O_4$@MnO–rGO nanocomposites

Samples	Surface area (m^2/g)	Total pore volume (cm^3/g)	Average pore diameter (nm)
GO	5.86	0.03722	25.37
rGO	11.01	0.05296	19.24
$ZnFe_2O_4$@MnO	75.54	0.203	10.74
$ZnFe_2O_4$@MnO–GO	26.77	0.1207	18.03
$ZnFe_2O_4$@MnO–rGO	14.08	0.06631	18.83

functional group. This is supported by the improved photocatalytic efficiency of the synthesized $ZnFe_2O_4$@MnO–GO nanocomposite compared to $ZnFe_2O_4$@MnO–rGO nanocomposite under the visible light [36].

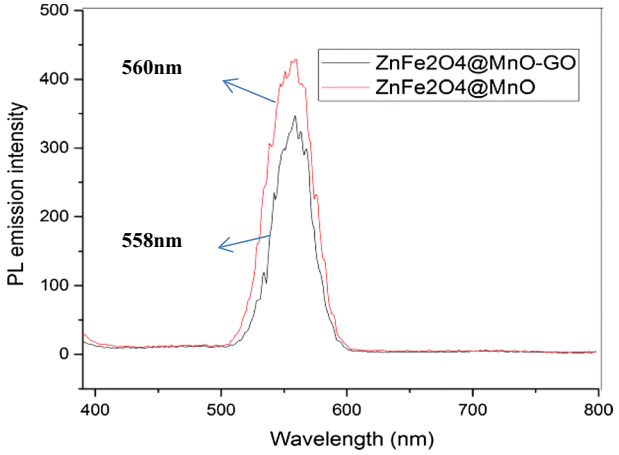

Fig. 20 Photoluminescence spectra of $ZnFe_2O_4$@MnO and $ZnFe_2O_4$@MnO–GO nanocomposites

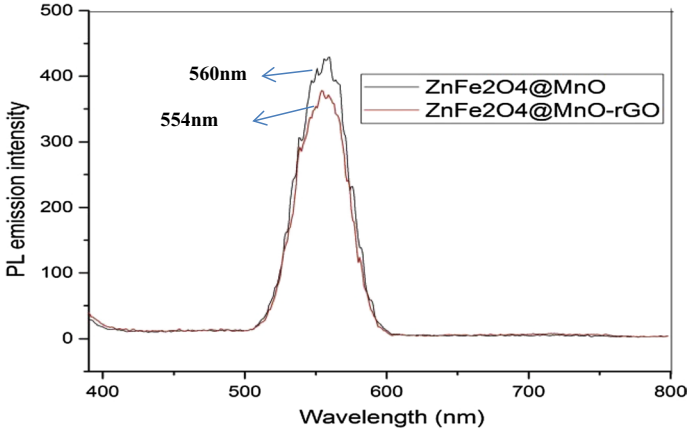

Fig. 21 Photoluminescence spectra of $ZnFe_2O_4$@MnO and $ZnFe_2O_4$@MnO–rGO nanocomposites

Photocatalytic degradation activities and kinetics of CR

The $ZnFe_2O_4$@MnO, $ZnFe_2O_4$@MnO–GO and $ZnFe_2O_4$@MnO–rGO nanocomposites are used for the photocatalytic degradation of CR under visible light irradiation, as shown in Figs. 22, 23 and 24. In this regard, 100 ml of 10 mg/l CR solution with time intervals of (5–35 min) at pH = 4 in the presence of 0.10 g ZnFe2O4@MnO, $ZnFe_2O_4$@MnO–GO and $ZnFe_2O_4$@MnO–rGO nanocomposites was exposed to the visible light. The results demonstrated that the percentage of maximum dye degradation in the presence of 0.10 g ZnFe2O4@MnO, $ZnFe_2O_4$@MnO–GO and $ZnFe_2O_4$@MnO–rGO nanocomposites was 96.21%, 98.73% and 95.98%, respectively. To investigate the effect of pH, several tests were performed on photocatalyst.

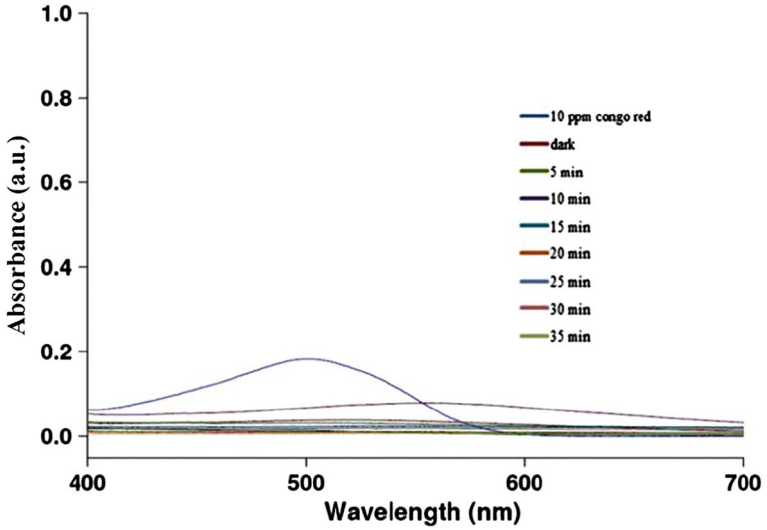

Fig. 22 Photocatalytic degradation of Congo red under visible light in the presence of $ZnFe_2O_4$@MnO. (Color figure online)

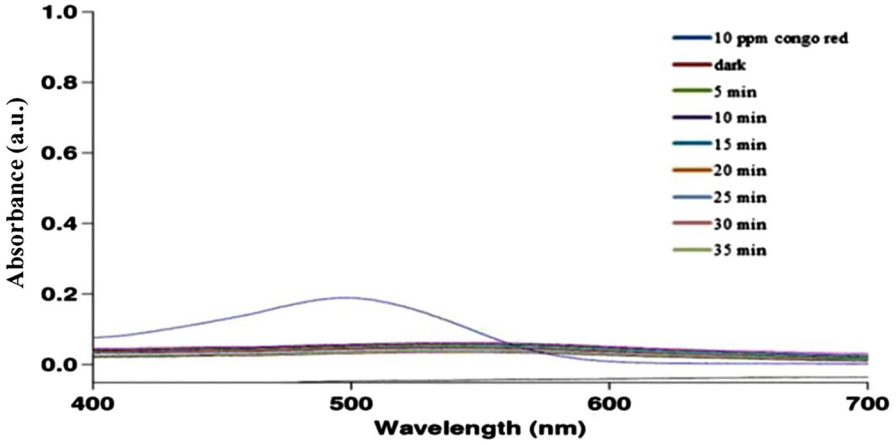

Fig. 23 Photocatalytic degradation of Congo red under visible light in the presence of $ZnFe_2O_4$@MnO–GO. (Color figure online)

The pH of 10 mg/l CR dye solution is about 7 in the presence of nanocomposite. Evaluation of the effect of pH was carried out in the range of 1–14 by using sodium hydroxide and hydrochloric acid. In the case studies, it was demonstrated that in the pH = 4, all photocatalysts can only degrade the Congo red, but it does not have the degradation ability, and the least photocatalytic activity was observed in the pH regions 5–12 and 1–3, respectively. The experiments of photocatalysis were carried out at pH = 4; due to this; pH is optimized, and nanocomposites gave the best efficiency in the photocatalytic degradation of Congo red. The effect of initial dye (CR),

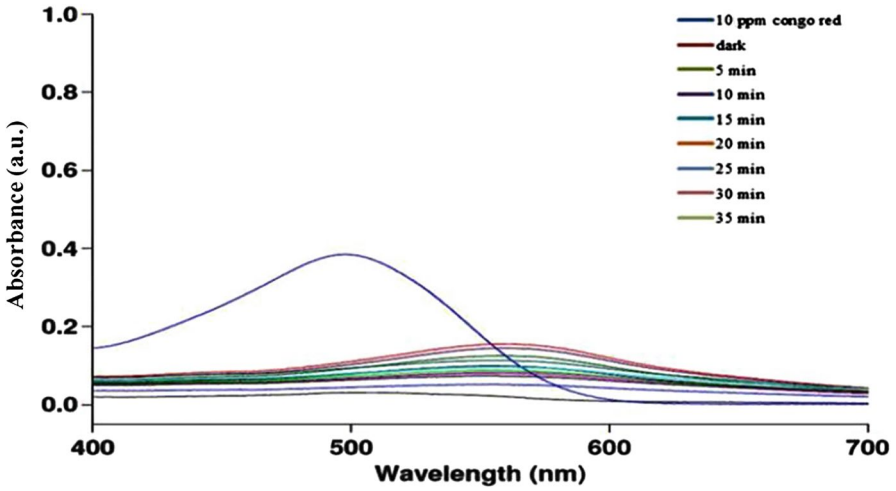

Fig. 24 Photocatalytic degradation of Congo red under visible light in the presence of $ZnFe_2O_4$@MnO–rGO. (Color figure online)

concentration on its photodegradation was investigated from 10 to 70 ppm at pH = 4 and nanocomposites dosage of 0.10 g/l. It is demonstrated that the photodegradation decreases with increase in initial CR concentration. At high dye concentrations, the formation reactive oxygen species on the photocatalyst surface is reduced because the photons are interrupted by the dye molecules before they can reach the catalyst surface. Further, nanocomposites dosage is also same for all initial CR concentration, and therefore the formation of $OH^{\cdot}$ remains constant [38]. In the case studies, at high dye concentrations, it does not have the degradation ability, and the least photocatalytic activity was observed; we do not mention in this study. The experiments of photocatalysis were carried out in 10 mg/l CR solution; due to this, concentration is optimized and nanocomposites gave the best performance in the photocatalytic degradation of Congo red.

Further, the reaction kinetics of the photocatalysis improved by using the first-order kinetic model as follows:

$$\ln C_t = \ln C_o - kt \tag{2}$$

where C_o and C_t represent the initial CR concentration and CR concentration at t time, respectively. The plot of ln (C_t/C_o) versus t can be approached as straight lines, as shown in Fig. 25a and b, which means that the photodegradation of CR is fitted as pseudo-first-order kinetics. Table 4 indicates the evaluated rate constant and the correlation coefficient under different conditions. The effect of the reaction rate of 0.10 g/l $ZnFe_2O_4$@MnO–GO was 0.063 min^{-1}, which was slightly higher, compared to 0.05 g/l and 0.02 g/l $ZnFe_2O_4$@MnO–GO nanocomposite. Furthermore, the effect of the reaction rate of 0.10 g/l $ZnFe_2O_4$@MnO–rGO was 0.059 min^{-1}, which was some higher, compared to 0.05 g/l and 0.02 g/l the prepared $ZnFe_2O_4$@MnO–rGO sample. The photocatalytic degradation of Congo red as a function of time by employing the synthesized ZnFe2O4@MnO, $ZnFe_2O_4$@MnO–GO and

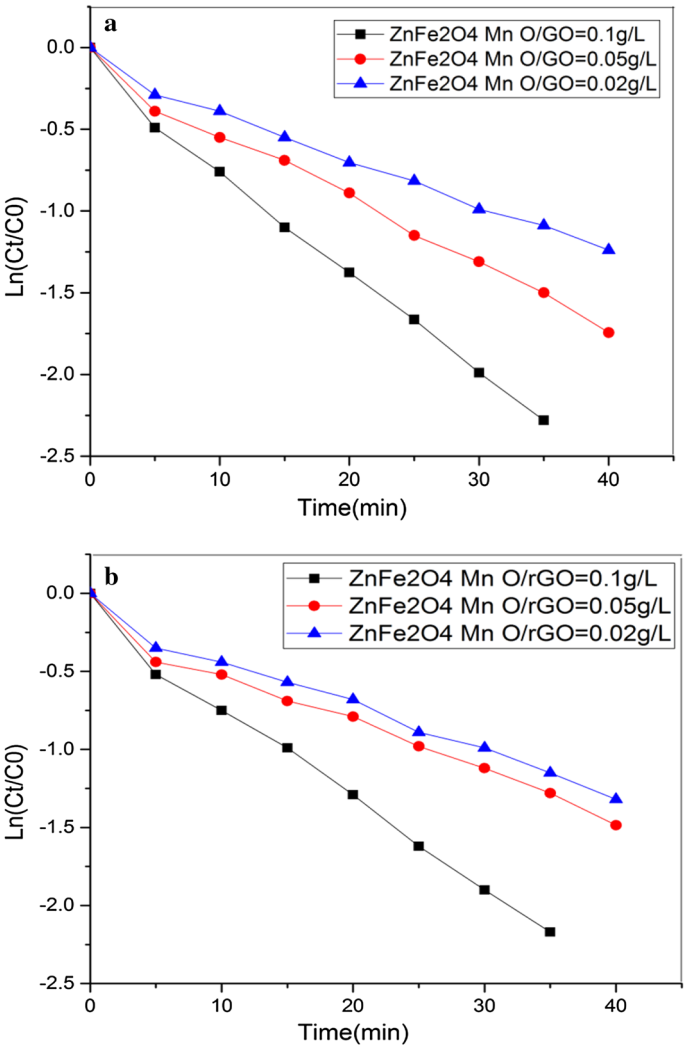

Fig. 25 **a** The effect of $ZnFe_2O_4$@MnO–GO catalyst amount on the photocatalytic degradation of Congo red. **b** The effect of $ZnFe_2O_4$@MnO–rGO catalyst amount on the photocatalytic degradation of Congo red. (Color figure online)

$ZnFe_2O_4$@MnO–rGO nanocomposites was studied under visible light irradiation, as shown in Fig. 26. It can be demonstrated that the $ZnFe_2O_4$@MnO–GO nanocomposites compared to $ZnFe_2O_4$@MnO nanocomposites gave the best efficiency in the photocatalytic degradation of Congo red. Also, it can be indicated that the $ZnFe_2O_4$@MnO nanocomposites compared to ZnFe2O4@MnO–rGO nanocomposites gave the best efficiency in the photocatalytic degradation of Congo red. The $ZnFe_2O_4$@MnO–GO nanocomposite gave the highest photocatalytic efficiency due to the well optical absorptions in the UV–Vis region with a lower band gap energy

Table 4 Rate constant of reaction kinetic for $ZnFe_2O_4$@MnO–GO and $ZnFe_2O_4$@MnO–rGO photocatalytic degradation by Congo red in different concentrations

Photocatalyst	Initial CR solution concentration (mg/l)	Photocatalyst loading (g)	k (min^{-1})	R^2
$ZnFe_2O_4$@MnO–GO	10	0.10	0.063	0.9951
$ZnFe_2O_4$@MnO–GO	10	0.05	0.041	0.9912
$ZnFe_2O_4$@MnO–GO	10	0.02	0.029	0.9894
$ZnFe_2O_4$@MnO–rGO	10	0.10	0.059	0.9925
$ZnFe_2O_4$@MnO–rGO	10	0.05	0.033	0.9744
$ZnFe_2O_4$@MnO–rGO	10	0.02	0.030	0.9833

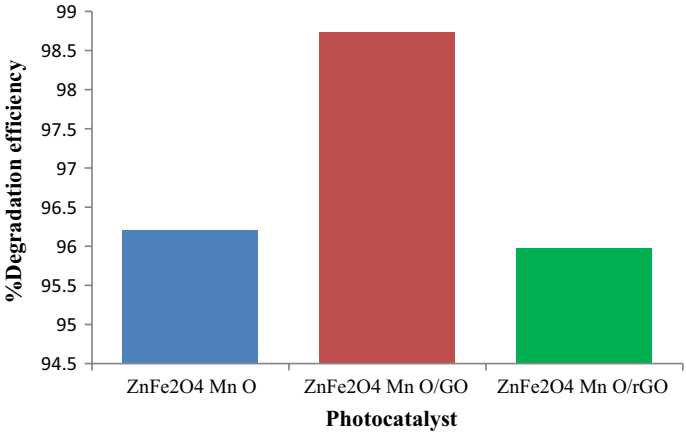

Fig. 26 Comparison of the photodegradation efficiencies of Congo red for $ZnFe_2O_4$@MnO, $ZnFe_2O_4$@MnO–GO and $ZnFe_2O_4$@MnO–rGO nanocomposites under visible light irradiation for 35 min. (Color figure online)

and a larger surface area giving a rise to a higher photocatalytic activity. Additionally, the graphene oxide in the nanocomposite can act as an electron transfer channel to reduce the recombination of the photogenerated electron holes, leading to improved photoconversion efficiency [39, 40]. Also, in reduced graphene oxide, a large part of the oxygen functionalities are eliminated, which can be caused to an undesirable effect on the electrical conductivity and other physical properties of it and so, its photocatalytic efficiency has been reduced in the adsorption metal ions and finally leading to decreasing photocatalytic efficiency. The reasonable photodegradation mechanism by using prepared $ZnFe_2O_4$@MnO–GO nanocomposite is displayed in Fig. 27. The $ZnFe_2O_4$@MnO nanomaterials decorated on the surface of GO sheet of the composite maybe excited and induced photogenerated e^-/h^+ pairs under the visible light irradiation as shown in Eq. (3). The photogenerated electron gets migrate from the conduction band (CB) of $ZnFe_2O_4$@MnO nanoparticles to the surface of GO (Eq. 4), and reduced oxygen molecule results in the formation of superoxide radicals O_2^- (Eq. 5). Further, the electron insufficiency (hole) on valence

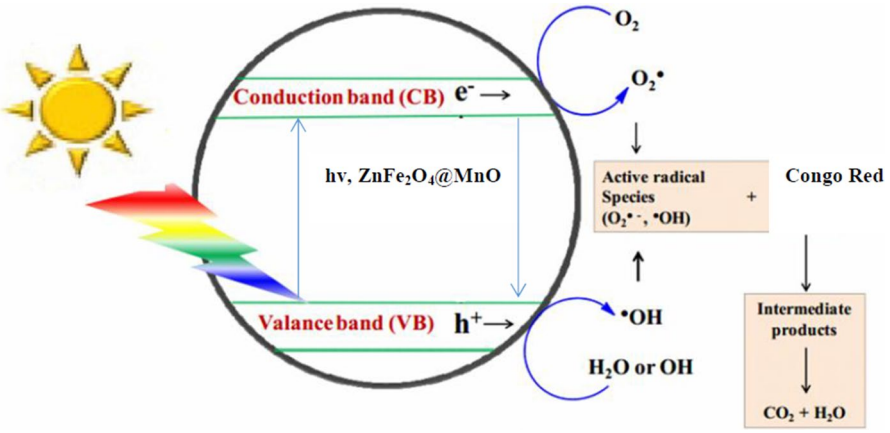

Fig. 27 Photocatalytic mechanism of $ZnFe_2O_4$@MnO–GO nanocomposite

band (VB) is accountable for the formation of hydroxyl radical ($OH^{\cdot}$) as given in Eq. (6). The key reactive species created during the photodegradation investigations specifically superoxide radicals (O_2^{-}) and hydroxyl radicals ($OH^{\cdot}$) are mostly liable for the degradation of organic pollutants into eco-friendly degradation product CO_2 and H_2O molecules (Eq. 8).

$$ZnFe_2O_4@MnO + hv \rightarrow ZnFe_2O_4@MnO(h^+) + ZnFe_2O_4@MnO(e^-) \quad (3)$$

$$ZnFe_2O_4@MnO\,(e^-)_{CB} + GO \rightarrow GO\,(e^-) + ZnFe_2O_4@MnO \quad (4)$$

$$GO\,(e^-) + O_2 \rightarrow GO + O_2^- \quad (5)$$

$$ZnFe_2O_4@MnO\,(h^+)_{VB} + OH^- \rightarrow ZnFe_2O_4@MnO + OH^{\cdot} \quad (6)$$

$$O_2^- + 2H_2O + e^- \rightarrow 3OH^- + OH^{\cdot} \quad (7)$$

$$O_2^- + OH^{\cdot} + CR \rightarrow CO_2 + H_2O \quad (8)$$

Effect of catalysts dosage

The photodegradation of CR dye onto $ZnFe_2O_4$@MnO–GO and $ZnFe_2O_4$@MnO–rGO nanocomposites was performed by verifying the amount of catalyst (0.1 g/l, 0.05 g/l, 0.02 g/l). The influence of catalyst concentration on the photodegradation ability is shown in Figs. 28 and 29. The photodegradation efficiency of CR is 98.73%, 83.51%, 73.31%, at 0.1 g/l, 0.05 g/l, 0.02 g/l of $ZnFe_2O_4$@MnO–GO, respectively. Additionally, the photodegradation efficiency of CR is 95.98%, 82.35%, 72.43%, at 0.1 g/l, 0.05 g/l, 0.02 g/l of $ZnFe_2O_4$@MnO–rGO, respectively. The enhanced photocatalytic activity of $ZnFe_2O_4$@MnO–GO and $ZnFe_2O_4$@MnO–rGO nanocomposites is owing to the incorporation of $ZnFe_2O_4$@MnO on the GO and

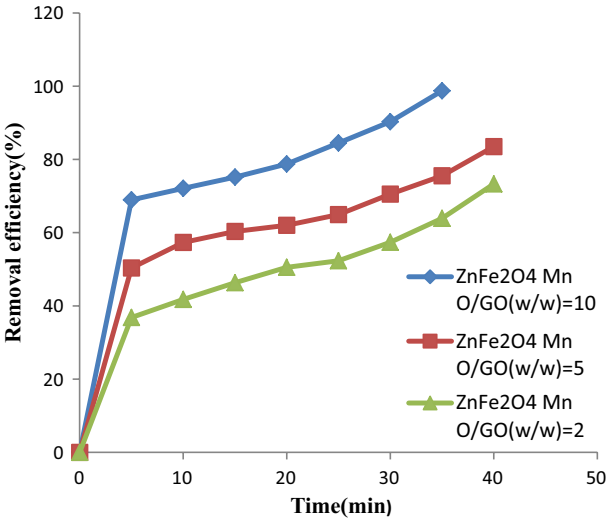

Fig. 28 Effect of loading $ZnFe_2O_4$@MnO–GO nanocomposite on the CR solutions degradation (Sample: 0.10 g $ZnFe_2O_4$@MnO–GO, initial concentration of CR solution: 10 mg/l, pH of CR solution: 4, Volume: 100 ml

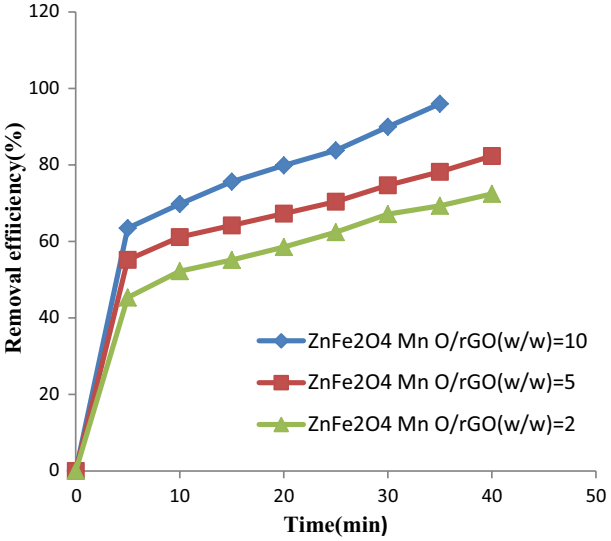

Fig. 29 Effect of loading $ZnFe_2O_4$@MnO–rGO nanocomposite on the CR solutions degradation (Sample: 0.10 g $ZnFe_2O_4$@MnO–rGO, initial concentration of CR solution: 10 mg/l, pH of CR solution: 4, Volume: 100 ml)

rGO sheets which amplifies separation of e^-/h^+ pairs and also, when the weight ratio of GO and rGO to [$ZnFe_2O_4$@MnO] increased, the degradation efficiency increased. This phenomenon is due to the efficient separation of the electron–hole

pairs, which prevented the recombination rate of e^-/h^+ pairs and enhances the photocatalytic degradation rate of pollutants. The comparative photocatalytic study of as-synthesized ZnFe2O4@MnO, $ZnFe_2O_4$@MnO–GO and $ZnFe_2O_4$@MnO–rGO nanocomposites by using CR dye solution under ambient reaction condition is given in Table 5. The optimized concentration of 0.10 g synthesized catalysts was elected for further photodegradation studies.

Conclusion

In conclusion, we synthesized magnetically separable $ZnFe_2O_4$@MnO–GO and $ZnFe_2O_4$@MnO–rGO photocatalysts via facile hydrothermal method at room temperature. The photocatalysts were studied by TEM, FESEM, EDAX, XRD, UV-DRS, BET, PL and VSM. FESEM, EDAX and TEM results demonstrated that graphene oxide sheets and reduced graphene oxide sheets were fully decorated with $ZnFe_2O_4$@MnO nanoparticles. Product photocatalytic activity was investigated in detail by photocatalytic degradation of Congo red dye under visible light irradiation. The photocatalytic experimental results indicated that $ZnFe_2O_4$@MnO, $ZnFe_2O_4$@MnO–GO and $ZnFe_2O_4$@MnO–rGO degrade Congo red dye in the same reaction condition by 96.21%, 98.73% and 95.98%, respectively. Based on our investigations and attained experimental results, we demonstrated that the combination of ZnFe2O4@MnO nanoparticles with the graphene oxide sheets revealed highly active catalyst for the degradation of Congo red under visible light irradiation. Highest photocatalytic activity was observed for the $ZnFe_2O_4$@MnO–GO (catalyst-0.10 g/l, dye concentration 10 mg/l and pH = 4). The decreasing PL emission intensity of $ZnFe_2O_4$@MnO–GO nanocomposite proposed the good interaction between $ZnFe_2O_4$@MnO and GO, which improved the electron–hole separation, leading to enhanced photocatalytic activity. The combination of the adsorption property of the graphene oxide nanosheet and the magnetic and photocatalytic property of $ZnFe_2O_4$@MnO–GO nanocomposite compared to $ZnFe_2O_4$@MnO–rGO nanocomposite makes the photocatalyst promising candidates for the solution of a variety of environmental problems. We hope that this article provides a path for researchers

Table 5 Comparative study of photocatalytic degradation by using optimized concentration of Congo red dye solution (50 mg/l)

Photocatalyst	Initial CR solution concentration (mg/l)	Photocatalyst loading (g)	Time (min) %	Degradation
$ZnFe_2O_4$@MnO	10	0.10	35	96.21
$ZnFe_2O_4$@MnO–GO	10	0.10	35	98.73
$ZnFe_2O_4$@MnO–GO	10	0.05	40	83.51
$ZnFe_2O_4$@MnO–GO	10	0.02	40	73.31
$ZnFe_2O_4$@MnO–rGO	10	0.10	35	95.98
$ZnFe_2O_4$@MnO–rGO	10	0.05	40	82.35
$ZnFe_2O_4$@MnO–rGO	10	0.02	40	72.43

into the improvement of nanocomposites photocatalytic activity in a shorter time with less cost.

Acknowledgements We thank science and research Branch, Islamic Azad University Tehran for supporting this study and Iran Nanotechnology Initiative.

References

1. M. Batool, M.Z. Qureshi, F. Hashmi, N. Mehboob, A.S. Shah, Indones. J. Chem. **19**(3), (2019)
2. R.S. Das, S.K. Warkhade, A. Kumar, A.V. Wankhade, Res. Chem. Intermed. **45**, 1 (2019)
3. G.M. Walker, L.R. Weatherley, Water Res. **31**(8), 2093 (1997)
4. B. Acemioğlu, J. Colloid Interface Sci. **274**(2), 371 (2004)
5. E.S. Agorku, A.T. Kuvarega, B.B. Mamba, A.C. Pandey, A.K. Mishra, J. Rare Earths **33**(5), 498 (2015)
6. S.O. Oppong, W.W. Anku, S.K. Shukla, P.P. Govender, Res. Chem. Intermed. **43**(1), 481 (2017)
7. P. Bakhtkhosh, A. Mehrizad, J. Mol. Liq. **240**, 65 (2017)
8. F. Tran, P. Blaha, Phys. Rev. Lett. **102**(22), 226401 (2009)
9. X. Liu, C. Chen, Y. Zhao, B. Jia, J. Nanomater. **2013**, 1 (2013)
10. M.M.A. Sinthiya, K. Ramamurthi, S. Mathuri, T. Manimozhi, N. Kumaresan, M.M. Margoni, P.C. Karthika, Int. J. Chem. Tech. Res. **7**, 2144 (2015)
11. M. Gurumoorthy, K. Parasuraman, M. Anbarasu, K. Balamurugan, Nano Vis. **5**, 63 (2015)
12. H. Zhang, X. Lv, Y. Li, Y. Wang, J. Li, ACS Nano **4**(1), 380 (2009)
13. L. Sun, J. Li, C. Wang, S. Li, Y. Lai, H. Chen, C. Lin, J. Hazard. Mater. **171**(1–3), 1045 (2009)
14. H. Huang, D. Li, Q. Lin, W. Zhang, Y. Shao, Y. Chen, X. Fu, Environ. Sci. Technol. **43**(11), 4164 (2009)
15. L. Huang, F. Peng, H. Wang, H. Yu, Z. Li, Catal. Commun. **10**(14), 1839 (2009)
16. R.S. Das, S.K. Warkhade, A. Kumar, A.V. Res, Chem. Intermed. **45**, 1 (2019)
17. V.K. Gupta, T. Eren, N. Atar, M. Lütfi Yola, C. Parlak, H. Karimi-Maleh, J. Mol. Liq. **208**, 122 (2015)
18. E.S. Agorku, A.C. Pandey, B.B. Mamba, A.K. Mishra, Mater. Today Proc. **2**(7), 3909 (2015)
19. M. Mzoughi, W.W. Anku, S.O. Oppong, S.K. Shukla, E.S. Agorku, P.P. Govender, Adv. Mater. Lett. **7**(12), 946 (2016)
20. S.B. Narde, R.B. Lanjewar, S.M. Gadegone, M.R. Lanjewar, Der Pharma Chem. **9**(7), 115 (2017)
21. F. Ciesielczyk, W. Szczekocka, K. Siwińska-stefańska, A. Piasecki, Open Chem. **15**, 7 (2017)
22. A. Thakur, S. Kumar, V.S. Rangra, Synthesis of reduced graphene oxide (rGO) via chemical reduction. in *AIP Conference Proceedings*, vol. 1661, no. 1, p. 080032 (2015)
23. C. Suwanchawalit, V. Somjit, Dig. J. Nanomater. Biostruct. **10**, 769 (2015)
24. B. Aslibeiki, P. Kameli, H. Salamati, J. Nanoparticle Res. **1–12**, 15 (2013)
25. F.Y. Ban, S.R. Majid, N.M. Huang, H.N. Lim, Int. J. Electrochem. Sci. **7**(5), 4345 (2012)
26. V. Loryuenyong, K. Totepvimarn, P. Eimburanapravat, W. Boonchompoo, A. Buasri, Adv. Mater. Sci. Eng. **2013**, 1 (2013)
27. K. Krishnamoorthy, G.-S. Kim, S.J. Kim, Ultrason. Sonochem. **20**, 644 (2013)
28. M.G. Naseri, E.B. Saion, Crystalization in spinel ferrite nanoparticles. In *Advances in Crystallization Processes*. IntechOpen (2012)
29. P. Sathishkumar, R.V. Mangalaraja, S. Anandan, M. Ashokkumar, Chem. Eng. J. **220**, 302 (2013)
30. H. Guo, J. Chen, W. Weng, Q. Wang, S. Li, Chem. Eng. J. **239**, 192 (2014)
31. K. Woan, G. Pyrgiotakis, W. Sigmund, Adv. Mater. **21**(21), 2233 (2009)
32. R. Leary, A. Westwood, Carbon **49**(3), 741 (2011)
33. P.V. Kamat, M. Gevaert, K. Vinodgopal, J. Phys. Chem. B **101**(22), 4422 (1997)
34. W. Wang, P. Serp, P. Kalck, J.L. Faria, J. Mol. Catal. A: Chem. **235**(1–2), 194 (2005)
35. Y. Zhang, N. Zhang, Z.R. Tang, Y.J. Xu, ACS Nano **6**(11), 9777 (2012)
36. S.O.B. Oppong, W.W. Anku, S.K. Shukla, P.P. Govender, Res. Chem. Intermed. **43**, 481 (2017)
37. R. Karthik, J.V. Kumar, S.-M. Chen, P.S. Kumar, V. Selvam, V. Muthuraj, Sci. Rep. **7**, 7254 (2017)

38. R. Arunadevi, B. Kavitha, M. Rajarajan, A. Suganthi, A. Jeyamurugan, Surfaces Interfaces **10**, 32 (2018)
39. D. Wang, X. Li, J. Chen, X. Tao, Chem. Eng. J. **198**, 547 (2012)
40. K. Ullah, L. Zhu, Z.D. Meng, S. Ye, Q. Sun, W.C. Oh, Chem. Eng. J. **231**, 76 (2013)

Affiliations

Azam Zamani[1] · Mirabdullah Seyed Sadjadi[1] · Alireza Mahjoub[2] · Mohammad Yousefi[1] · Nazanin Farhadyar[3]

✉ Mirabdullah Seyed Sadjadi
m.s.sadjad@gmail.com

Azam Zamani
Azamani646@gmail.com

Alireza Mahjoub
mahjouba@modares.ac.ir

Mohammad Yousefi
myousefi50@hotmail.com

Nazanin Farhadyar
quantomlife@gmail.com

[1] Department of Chemistry, Science and Research Branch, Islamic Azad University, Tehran, Iran

[2] Department of Chemistry, Tarbiat Modares University, Tehran, Iran

[3] Department of Chemistry, Varamin Pishva Branch, Islamic Azad University, Varamin, Iran